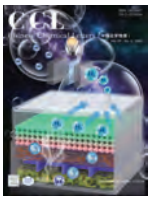
Chinese Chemical Letters 37 (2026) 111141

Contents lists available at ScienceDirect

Chinese Chemical Letters

journal homepage: www.elsevier.com/locate/cclet



Augmenting heptamethine cyanine photosensitivity while retaining strong fluorescence emission: Forming dye-albumin nanocomplex enables tumor-targeted photodynamic therapy

Mengxing Liu, Jing Liu*, Hongxing Zhang*, Lijuan Wang, Jianan Tao, Wei Guo*

School of Chemistry and Chemical Engineering, Shanxi University, Taiyuan 030006, China

ARTICLE INFO

Article history:
Received 23 January 2025
Revised 15 March 2025
Accepted 25 March 2025
Available online 25 March 2025

Keywords:
Tumor
Photodynamic therapy
Heptamethine cyanine
Albumin
Nanocomplex

ABSTRACT

In this work, the spin-orbit charge transfer intersystem crossing (SOCT-ISC) mechanism is introduced into the near-infrared and highly photon-capturing heptamethine cyanine (Cy7) class to construct photosensitizer (PS) for photodynamic therapy (PDT) of tumor. The target PS AN–Cy7 shows an obviously improved singlet oxygen ($^1O_2$) quantum yield than the Food and Drug Administration (FDA)-approved indocyanine green (ICG) under 750 nm low-power photoirradiation (30 mW/cm^2) while retaining strong fluorescence at ~805 nm. Importantly, the PS forms a 2:1 dye-human serum albumin (HSA) nanocomplex, ensuring its strong accumulation and retention at tumor site (up to five days) post intravenous injection. After a single PDT treatment, the nanocomplex almost completely ablates primary tumor while triggering an antitumor immune response to suppress the growth of distant tumors. Overall, the nanocomplex overcomes many shortcomings of clinically used PSs, thus being promising for future clinical translation.

© 2026 Published by Elsevier B.V. on behalf of Chinese Chemical Society and Institute of Materia Medica, Chinese Academy of Medical Sciences.

Photodynamic therapy (PDT) is a clinically approved, photochemistry-regulating therapeutic modality for various diseases, especially cancers, which utilizes photosensitizer (PS), light, and molecular oxygen ($^3O_2$) to induce phototoxicity by generating cytotoxic reactive oxygen species (ROS), such as singlet oxygen ($^1O_2$), superoxide ($O_2^{\bullet-}$), and hydroxyl radical ($HO^{\bullet}$). Compared with the traditional cancer treatment protocols, PDT enjoys many advantages, including high spatiotemporal precision, non-invasiveness, negligible drug resistance, and activation of immunogenic cell death, and thus has attracted considerable attention in the past decade [1–7]. Central to the therapeutic modality is PS, whose ROS-generating ability in principle relies on the population of a long-lived triplet excited state (T_1) from singlet excited state (S_1) *via* intersystem crossing (ISC). Early PSs are primarily focused on porphyrin derivatives, which, although broadly used in clinic, suffer from several disadvantages, such as short excitation wavelength (commonly <660 nm), poor photon-capturing ability, complicated synthesis, and insufficient tumor targetability [8]. In addition to porphyrin derivatives, a popular approach in designing PS is introducing heavy atom to dye skeleton that promotes $S_1 \rightarrow T_1$ ISC by importing strong spin-orbital coupling (SOC). However, heavy atom also simultaneously promotes $T_1 \rightarrow S_0$ (ground state) ISC, and thus this type of PSs commonly has short T_1-state lifetimes, which, coupled with the potential cytotoxicity of heavy atom, hinders their widespread applications. Indeed, the concern has compelled considerable research efforts into the heavy-atom-free PSs in recent years by exploiting alternative ISC mechanisms, typically including reducing S_1-T_1 energy gap, symmetrically allowed $S_1(n, \pi^*) \rightarrow T_1(\pi, \pi^*)$ transition, radical-enhanced ISC (RE-ISC), twisted π-conjugation-induced ISC, and spin-orbit charge transfer ISC (SOCT-ISC) [9–11]. Even so, the excitation wavelengths of most of these heavy-atom-free PSs are below the phototherapeutic window of 650–900 nm [12], thus unfavorable for treating the deep-seated tumor tissue. Considering that the penetration depth of 800 nm light is twice that of 630 nm [1] and that the irradiation light above 850 nm cannot commonly provide enough energy to produce $^1O_2$ [13], the development of the heavy-atom-free PS with excitation wavelength in the wavelength range of 750–850 nm is highly desirable [14].

The consideration turned our attention to heptamethine indocyanine (Cy7) dyes, since the dye class enjoys not only the near-infrared (NIR, 700–900 nm) absorption and emission maxima of 750–850 nm, but also the exceptionally large molar extinction coefficients ($>2.0 \times 10^5$ L mol^{-1} cm^{-1}) [15–20] when compared with visible boron–dipyrromethenes (BODIPYs) or rhodamine dyes [21]. Moreover, some Cy7 dyes have been reported to be able to form

* Corresponding authors.
E-mail addresses: liujing4203@sxu.edu.cn (J. Liu), hxzhang4714@sxu.edu.cn (H. Zhang), guow@sxu.edu.cn (W. Guo).

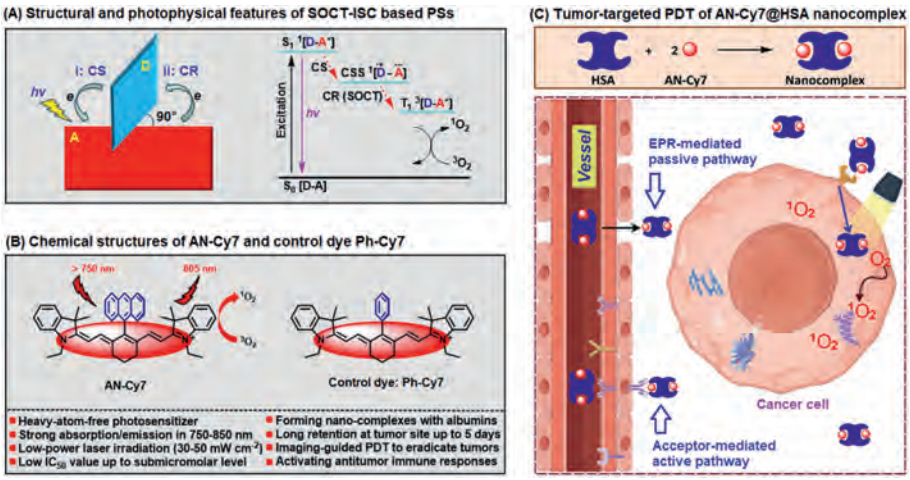
https://doi.org/10.1016/j.cclet.2025.111141
1001-8417/© 2026 Published by Elsevier B.V. on behalf of Chinese Chemical Society and Institute of Materia Medica, Chinese Academy of Medical Sciences.

nanocomplexes with native serum albumins, thereby displaying strong tumor targetability [22–27] due to the enhanced permeability and retention (EPR) effect as well as the overexpressed albumin receptors, including glycoproteins (Gp18, Gp30 and Gp60) and secreted protein acidic rich in cysteine (SPARC), in various tumor tissues [28–30]. As a typical representative, indocyanine green (ICG) is a Food and Drug Administration (FDA)-approved NIR optical marker for clinical imaging uses, which exhibits some PDT activity but with a low $^1O_2$ quantum yield ($\Phi_\Delta = 0.008$ in MeOH) [31]. Indeed, to date, introducing heavy atoms is still a main tactic to endow the dye class with photosensitivity [14,32–39]. Although a heavy-atom-free Cy7 PS was recently exploited based on the RE-ISC mechanism, the PS structurally belongs to *meso*–amino Cy7 series, thus exhibiting a short absorption maximum of <650 nm [40]. In addition, several heavy-atom-free Cy7 dyes, although bearing no obvious structural feature to favour ISC for populating T_1 state, were also reported to be capable of producing $^1O_2$ under the high-power laser irradiation [25,41–44]. Considering that the high-power laser could make a fraction of fluorophores being trapped in triplet state [45], the observed $^1O_2$ generation of these Cy7 dyes under photoirradiation is understandable, and indeed their cancer cell-killing capabilities primarily result from the photothermal effect under the high-power laser irradiation (commonly 0.5–1.5 W/cm^2). To avoid the high-power laser-caused photodamage to healthy tissues and photobleaching to PSs, the development of the heavy-atom-free Cy7 PSs, characterized by the high photosensitivity under the low-power laser irradiation [37,39], is urgently needed. And to do that, a well-defined ISC mechanism should first be identified to augment their photosensitivity in producing ROS.

Among various ISC mechanisms for constructing the heavy atom-free PSs, the SOCT-ISC mechanism has caught much attentions in recent years [46–59]. As shown in Scheme 1A, the type of PSs is composed of the closely linked and orthogonal electron donor (D) and acceptor (A, commonly a chromophore) dyad, and the corresponding photophysics involves a light-driven charge separation (CS) and recombination (CR) cascade between D and A that effectively populates T_1 state. Inspired by the mechanism, we envisioned that, by installing a bulky electron donor to the *meso*–position of Cy7 skeleton, it is possible to achieve a SOCT-ISC-based Cy7 PS. Recently, we presented a one-pot cyanine-ketone method for accessing the robust *meso*–aryl Cy7 dyes [60], by which a *meso*–anthranyl Cy7 dye, *i.e.*, AN–Cy7, was also prepared (Scheme 1B). Considering that anthranyl group, as an electron donor, has widely been used to construct the SOCT-ISC-based PSs [48,51,58], the Cy7 dye was greatly expected to be a PS operating *via* such mechanism. In this work, we confirmed the role of AN–Cy7 as a SOCT-ISC-based PS by theoretical calculations and experimental evidences, and found that the PS displayed a 14-fold higher $^1O_2$-generating efficacy than ICG under 750 nm low-power laser irradiation while retaining strong fluorescence at ~805 nm. Further, we found that the PS formed a 2:1 nanocomplex with human serum albumin, and showed strong accumulation and retention at tumor site (Scheme 1C). *In vivo* PDT assays revealed that, under 750 nm photoirradiation, the nanocomplex almost completely ablated primary tumors while triggering an antitumor immune response to efficiently suppress the growth of distant tumors.

AN–Cy7 and Ph–Cy7 (a control dye) were synthesized according to our previously reported procedures [60]. The absorption and emission spectra of the two Cy7 dyes were shown in Fig. S1 (Supporting information), and the corresponding photophysical properties were summarised in Table S1 (Supporting information). As seen, in CH_2Cl_2, AN–Cy7 exhibited an intense absorption band peaked at 775 nm with the molar extinction coefficient (ε) even up to 3.48×10^5 L mol^{-1} cm^{-1}, indicative of its strong photon-capturing ability as well as the strong tissue penetrability of its irradiation light. Moreover, AN–Cy7 also showed a strong fluorescence emission at 804 nm in the solvent with the fluorescence quantum yield (Φ_f) up to 0.32, almost identical to that of Ph–Cy7 ($\Phi_f = 0.33$). As a result, the fluorescence brightness ($\varepsilon \times \Phi_f$) of AN–Cy7 in CH_2Cl_2 was calculated to be as large as 111,000 L mol^{-1} cm^{-1}. Although in more polar CH_3CN or phosphate buffer saline (PBS)/CH_3CN, AN–Cy7 displayed decreased brightness (56,000 L mol^{-1} cm^{-1} in CH_3CN and 37,000 L mol^{-1} cm^{-1} in PBS/CH_3CN), it is still bright enough for the *in vitro* or *in vivo* fluorescence imaging applications.

To figure out whether AN–Cy7 could serve as a SOCT-ISC-based PS, we first conducted theoretical calculations using the time-dependent density functional theory (TDDFT) method. As seen in Fig. S2A (Supporting information), the calculation produced a S_2 state with a large oscillator strength ($f = 2.0903$), which could be assigned as the locally excited (LE) state given that electron and hole are both located on Cy7 unit. Importantly, the calculation also gave rise to a low-lying S_1 state, which could be assigned to the charge separation state (CSS) given that electron and hole are separated completely ($f = 0$) and located respectively on Cy7 and *meso*–anthranyl units [61]. Further, we calculated the triplet states of AN–Cy7 by setting the spin as triplet. It was found that energy gap



Scheme 1. (A) Orthogonal D-A construct for the SOCT-ISC-based PS and corresponding Jablonski diagram that illustrates the processes of T_1-state population *via* CS and CR and $^1O_2$ generation *via* energy transfer. (B) Chemical structures of AN–Cy7 and control dye Ph–Cy7 reported in this work. (C) Schematic illustration of the tumor-targeted PDT of the AN–Cy7-HSA nanocomplex.

(ΔE) between CSS and T_3 states is very small (ΔE: 0.2162 eV), indicative of the feasibility of CSS→T_3 ISC. Subsequent internal conversion (IC) would populate T_1 state. Notably, the calculation also revealed an orthogonal geometry between *meso*–anthranyl and Cy7 units, thus structurally facilitating AN–Cy7 to populate T_1 state in terms of the SOCT-ISC mechanism [46–59]. In stark contrast, the TDDFT calculation on Ph–Cy7 only gave rise to locally excited S_1 (LE) and S_2 (LE) states, and no energetically lower CSS state was observed (Fig. S2B in Supporting information). Thus, it should be difficult for Ph–Cy7 to populate T_1 state due to the absence of an electron donor. Encouraged by the calculations, the electron paramagnetic resonance spectrum of AN–Cy7 was measured under continuous photoirradiation at 173 K, which gave rise to a clear signal corresponding to an organic radical at ~3375 G (Fig. S3A in Supporting information), experimentally supporting the production of the radical-featured CSS state. Also, we performed femtosecond transient absorption spectra study of AN–Cy7. As seen in Fig. S3B (Supporting information), following a laser pulse, a negative ground state bleaching (GSB) band in the range of 560–780 nm and a positive excited-state absorption (ESA) band peaked at ~550 nm were generated. Although the ESA signal disappeared at *ca.* 1000 ps, the GSB signal remained even at 6 ns (the maximum time range of the device), indicative of the production of a long-lived excited state—most likely being the T_1 state due to its long lifetime [39]. Indeed, this could further be validated by the obvious $^1O_2$ generation under photoirradiation due to the T_1-T_1 energy exchange between O_2 and AN–Cy7 (Figs. 1A–C).

Subsequently, we evaluated the photosensitivity of AN–Cy7 and Ph–Cy7 in CH_2Cl_2 with commercial 1,3-diphenylbenzoisofuran (DPBF) as the $^1O_2$ scavenger. As shown in Fig. 1A, upon continuous photoirradiation of the AN–Cy7/DPBF solution under 750 nm low-power laser irradiation (30 mW/cm^2) for 450 s, a substantial amount of $^1O_2$ was observed, as indicated by the almost complete photobleaching of DPBF absorbance at 416 nm; by comparison, only a small amount of $^1O_2$ was produced for Ph–Cy7 in the otherwise identical condition (Fig. S4 in Supporting information). The $^1O_2$ quantum yields (Φ_Δ) of AN–Cy7 in CH_2Cl_2 was determined to be 0.114 using ICG ($\Phi_\Delta = 0.008$) as a reference [31], which is 14-fold greater than that of ICG, highlighting the importance of the *meso*-anthranyl electron donor in endowing Cy7 dye with markedly improved photosensitivity. The Φ_Δ value of AN–Cy7 in CH_2Cl_2 is similar to those of the previously reported *meso*-anthranyl Cy5 PSs that also operate *via* SOCT-ISC mechanism [58]. Notably, although AN–Cy7 shows a strong ability in generating $^1O_2$ under photoir-

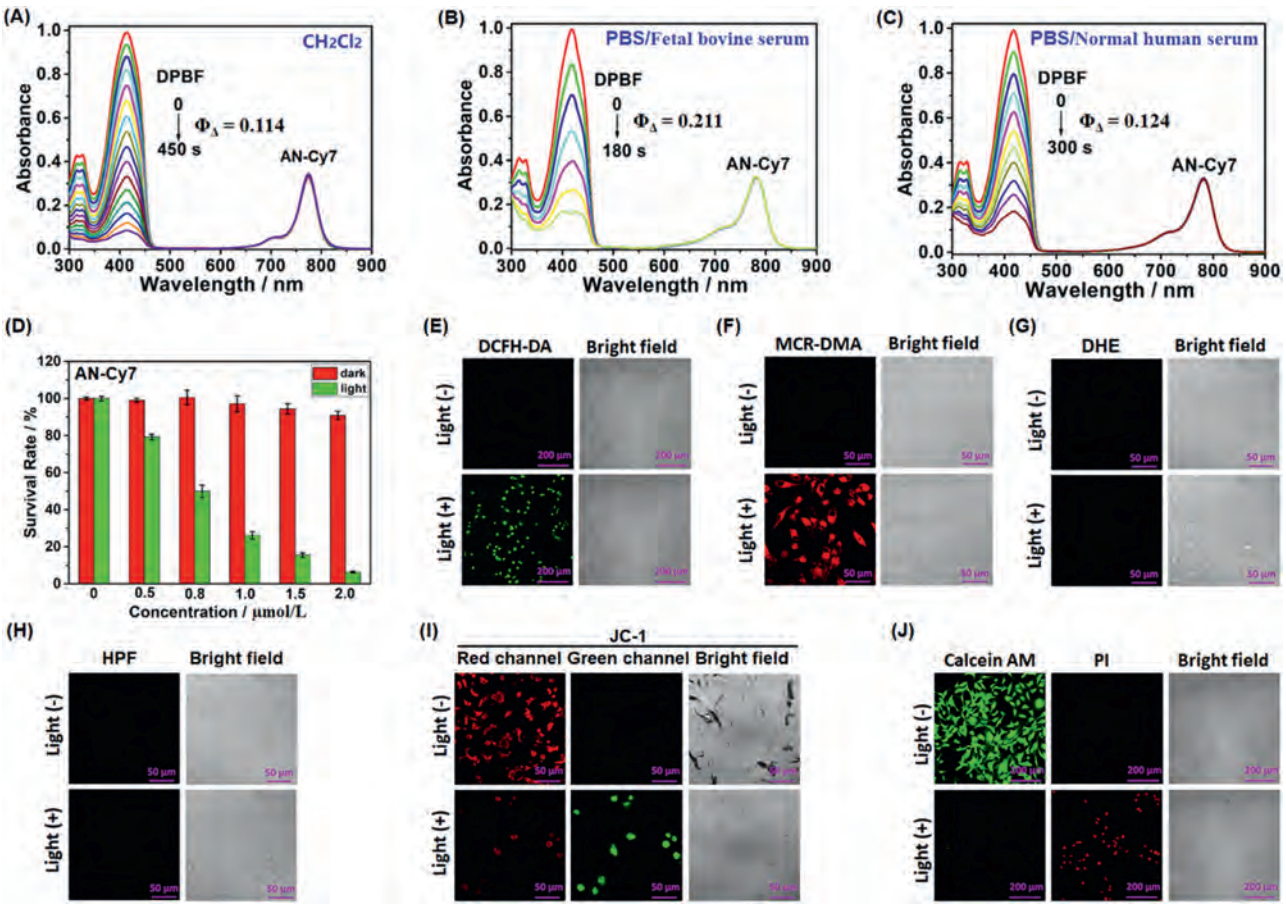


Fig. 1. (A–C) Absorption spectral changes of DPBF in the presence of AN–Cy7 in CH_2Cl_2 and PBS supplemented with 10% FBS or normal human serum under 750 nm laser irradiation (30 mW/cm^2). (D) Dose-dependent viability of the AN–Cy7-loaded A549 cells with and without 750 nm laser irradiation (30 mW/cm^2, 30 min). Data are presented as mean ± standard deviation (SD) ($n = 4$). (E) Confocal images of the AN–Cy7 (1.0 μmol/L)/DCFH-DA (10.0 μmol/L)-loaded A549 cells treated without and with 750 nm photoirradiation. For DCFH-DA, emission was collected in 500–750 nm ($\lambda_{ex} = 488$ nm). Scale bar: 200 μm. (F) Confocal images of the AN–Cy7 (1.0 μmol/L)/MCR-DMA (2.0 μmol/L)-loaded A549 cells treated without and with 750 nm photoirradiation. For MCR-DMA, emission was collected at 640–750 nm ($\lambda_{ex} = 633$ nm). Scale bar: 50 μm. (G) Confocal images of the AN–Cy7 (1.0 μmol/L)/DHE (10.0 μmol/L)-loaded A549 cells treated without and with 750 nm photoirradiation. For DHE, emission was collected at 500–730 nm ($\lambda_{ex} = 488$ nm). Scale bar: 50 μm. (H) Confocal images of the AN–Cy7 (1.0 μmol/L)/HPF (10.0 μmol/L)-loaded A549 cells treated without and with 750 nm photoirradiation. For HPF, emission was collected in 500–730 nm ($\lambda_{ex} = 488$ nm). Scale bar: 50 μm. (I) Confocal images of the AN–Cy7 (1.0 μmol/L)/JC-1 (10.0 μmol/L)-loaded A549 cells treated without and with 750 nm photoirradiation. For green channel (JC-1 monomer), emissions were collected at 490–560 nm ($\lambda_{ex} = 488$ nm); for red channel (JC-1 aggregate), at 570–750 nm ($\lambda_{ex} = 561$ nm). Scale bar: 50 μm. (J) Confocal fluorescence images of the AN–Cy7 (1.0 μmol/L)-loaded A549 cells treated with 750 nm photoirradiation and then co-stained with calcein AM/PI (2.0 μmol/L /4.5 μmol/L). For calcein AM, emission collected at 505–535 nm ($\lambda_{ex} = 488$ nm); for PI, at 590–700 nm ($\lambda_{ex} = 561$ nm). Scale bar: 200 μm.

radiation, its fluorescence property is not impacted by its *meso*-anthranyl electron donor when compared with Ph–Cy7. Conversely, for many heavy atom-based Cy7 PSs, their fluorescence is greatly quenched due to heavy atom effect [31–36]. We hypothesized that the bulky *meso*–anthranyl group, in addition to its role in promoting ISC to populate T_1 state, also largely decreases the nonradiative thermal decay, thereby considerably retaining the fluorescence of AN–Cy7 [37,58]. The speculation was supported by the obviously lower photothermal conversion efficiency (η) of AN–Cy7 (7.7%) than that of Ph–Cy7 (20.6%) under 750 nm photoirradiation (Fig. S5 in Supporting information).

However, distinct from the sharp monomer absorption in CH_2Cl_2, AN–Cy7 in PBS displayed a broadened absorption band in the wavelength range of 600–900 nm, accompanied by the greatly quenched fluorescence, indicative of the formation of AN–Cy7 aggregate in the condition (Fig. S6 in Supporting information). Moreover, the continuous 750 nm laser irradiation (30 mW/cm^2) of the PBS solution of AN–Cy7/ABDA (9′,10′-anthracenediyl-bis-(methylene)-dimalonic acid, a water soluble $^1O_2$ probe) led to obvious photobleaching of AN–Cy7 aggregate, accompanied by negligible $^1O_2$ generation (Fig. S7A in Supporting information); similar photobleaching was also observed in the absence of ABDA (Fig. S7B in Supporting information), indicating that AN–Cy7 aggregate is photo-unstable. Considering that some hydrophobic Cy7 dyes can form water-soluble and photostable dye-albumin complexes [22–27], the photophysical properties and photosensitivity of AN–Cy7 were further evaluated in PBS supplemented with 10% fetal bovine serum (FBS) that is known to contain an extremely high concentration of bovine serum albumin (BSA, *ca.* 35–50 mg/mL) [24]. To our delight, upon adding 10% FBS to the PBS solution of AN–Cy7, the broad aggregate absorption band disappeared, and instead a sharp monomer absorption band emerged, accompanied by a marked fluorescence enhancement, strongly indicative of the formation of AN–Cy7-BSA complex (Figs. S8A and B in Supporting information); moreover, no obvious photobleaching was observed under photoirradiation, indicative of the good photostability of AN–Cy7 in the PBS-serum system (Fig. S8C in Supporting information). Importantly, using DPBF as a $^1O_2$ indicator, it was found that AN–Cy7 shows a strong ability in generating $^1O_2$ in the PBS-serum system under 750 nm photoirradiation, and the corresponding Φ_Δ value was determined to be 0.211 (Fig. 1B), ~26-fold higher than that of ICG. Considering that human serum albumin (HSA) is structurally similar to BSA with 80% sequence homology [22], we also evaluated the $^1O_2$-generating ability of AN–Cy7 in PBS supplemented with 10% normal human serum (purchased from Sigma-Aldrich (Shanghai, China)). Like that found in the PBS-FBS system, the formation of AN–Cy7-HSA complex and its good photostability (Fig. S8D in Supporting information) were also revealed in the PBS-normal human serum system, and the corresponding Φ_Δ value was determined to be 0.124 (Fig. 1C), ~15-fold higher than that of ICG. Note that, DPBF is soluble in the two PBS-serum systems, thus suitable for evaluating the photosensitivity of AN–Cy7. Although ABDA is a hydrophilic $^1O_2$ indicator, it lost its reactivity with $^1O_2$ in the PBS-serum system (Fig. S9A in Supporting information), thus not suitable for evaluating the $^1O_2$ generation. The case was supported by the photosensitivity assays of a commercial type-II PS methylene blue (MB), where, although the absorbance of ABDA decreased markedly in PBS under photoirradiation (Fig. S9B in Supporting information), it remained almost unchanged in the PBS-serum system under the otherwise identical condition (Fig. S9C in Supporting information). Further, by absorption titration in PBS, the binding ratios of BSA and HSA to AN–Cy7 were determined to be ~2:1 and ~1:2, respectively (Figs. S10 and S11 in Supporting information). Notably, AN–Cy7-BSA and AN–Cy7-HSA complexes in PBS were both strong fluorescent with fluorescence quantum yields calculated to be 0.12 and 0.19, respectively. Also, using dihydrorhodamine 123 (DHR123, a fluorescent $O_2^{\bullet-}$ probe) and hydroxyphenyl fluorescein (HPF, a commercial specific fluorescent HO$^\bullet$ probe), we demonstrated that the photoirradiation of AN–Cy7 in the PBS-serum system does not produce $O_2^{\bullet-}$ and HO$^\bullet$ (Fig. S12 in Supporting information), meaning that AN–Cy7 is a typical energy transfer-dependent Type-II PS [2].

Next, we evaluated the *in vitro* PDT efficacy of AN–Cy7 in cancerous A549 cells using cell counting kit-8 (CCK8) assays. Before light irradiation, the cells were incubated with AN–Cy7 in the cell culture medium DMEM supplemented with 10% FBS at 37 °C for 60 min, and after light irradiation, the AN–Cy7-loaded A549 cells were further incubated in the cell culture medium for 24 h at 37 °C before CCK8 assay. As shown in Fig. 1D, AN–Cy7 showed low dark toxicity in the concentration range of 0–2 μmol/L; however, upon exposure to 750 nm low-power laser (30 mW/cm^2, 30 min), it efficiently inhibited cell proliferation in a dose-dependent manner with half maximal inhibitory concentration (IC_{50}) value as low as 0.8 μmol/L. Of note, the laser intensity used in the assays is much lower than the maximum permissible exposure (MPE) (0.33 W/cm^2 for 808 nm and 0.25 W/cm^2 for 750 nm) as well as those of most of the reported Cy7 PSs (0.5–1.5 W/cm^2) [25,41–44], meaning that the PDT activity of AN–Cy7 could efficiently be triggered by the safe laser intensity. Further, we performed the *in vitro* imaging assays to probe the AN–Cy7-mediated PDT mechanism. Using 2′,7′-dichlorodihydrofluorescein diacetate (DCFH-DA, a commercial fluorescent probe for total ROS), we confirmed that the PDT process induces a substantial amount of intracellular ROS, as indicated by the strong green fluorescence of AN–Cy7/DCFH-DA-loaded A549 cells after continuous irradiation by 750 nm laser (Fig. 1E); using a NIR fluorescent $^1O_2$ probe MCR-DMA developed by us previously [62], we confirmed that the PDT process markedly induces the generation of intracellular $^1O_2$ (Fig. 1F); using dihydroethidium (DHE, a commercial specific fluorescent $O_2^{\bullet-}$ probe) and HPF, we also confirmed that the PDT process does not produce intracellular $O_2^{\bullet-}$ and HO$^\bullet$, respectively (Figs. 1G and H), further confirming that AN–Cy7 is an energy transfer-dependent Type II PS. In addition, we performed the CCK8 assay after the AN–Cy7-loaded A549 cells were irradiated by 750 nm laser under ice incubation (for probing the photothermal effect), or after the cells were pretreated with *N*-acetylcysteine (NAC, an effective ROS scavenger) and then irradiated by 750 nm laser (for probing the PDT effect). It was found that the former results in an almost consistent cell death rate to that performed at 37 °C, and the latter obviously inhibits cell death (Fig. S13 in Supporting information), strongly indicating that PDT, rather than photothermal effect, plays a crucial role for AN–Cy7 to kill cancer cells. The PDT-induced mitochondrial depolarization, a characteristic of early apoptotic cells, was also verified by a commercial mitochondrial membrane potential probe JC-1 (red fluorescence: high membrane potential; green fluorescence: low membrane potentials) (Fig. 1I). Moreover, the PDT-induced cell death could intuitively be observed in the calcein-AM (green fluorescence: live cells)/propidium iodine (PI) (red fluorescence: dead cells) double staining assay (Fig. 1J). In addition, it was found that compared to normal LO2 cells, AN–Cy7 could preferentially be taken up by cancerous A549 cells in DMEM supplemented with 10% FBS (Fig. S14 in Supporting information), and displays a stronger killing efficacy to A549 cells than to normal LO2 cells under photoirradiation (Fig. S15 in Supporting information), meaning that AN–Cy7 could selectively kill cancer cells over normal cells with the help of serum albumin.

Before *in vivo* PDT assays, we prepared the PBS solutions of AN–Cy7-BSA and AN–Cy7-HSA complexes, termed AN–Cy7@BSA and AN–Cy7@HSA thereafter, by respectively adding BSA (3.0 equiv.) and HSA (0.75 equiv.) to the PBS solution of AN–Cy7 (50 μmol/L), followed by filtration through a 200-nm filter. The concentrations of BSA and HSA used here are ~1.5-fold higher

than the values derived from the binding ratios of BSA and HSA to AN–Cy7 (*i.e.*, 2:1 and 1:2, respectively) for ensuring sufficient encapsulation. With AN–Cy7 regarded as solute, the final concentrations of the two dye-albumin complexes were determined both to be around 48 μmol/L by absorption spectra. The formation of AN–Cy7@BSA and AN–Cy7@HSA nanocomplexes were confirmed by dynamic light scattering (DLS) assays with average hydrodynamic diameters determined to be 12 and 153 nm (zeta potentials: −4.6 and −11.1 mV, respectively), which could further be visualized by transmission electron microscope (TEM), where their average particle sizes were found to be 11 nm and 113 nm, respectively (Fig. S16 in Supporting information). The smaller particle sizes observed in TEM than those observed in DLS is due to the shrinkage of the hydration layer in the dried TEM samples. Given that nanoparticle within a size range of 20–200 nm is beneficial for accumulation at tumor site due to EPR effect [63], AN–Cy7@HSA was expected to have stronger tumor-targeting ability than AN–Cy7@BSA.

The tumor-targeting abilities of the two nanocomplexes were evaluated in the subcutaneous HepG2 tumor-bearing BALB/c mice. Animal experiment was carried out in accordance with the relevant laws and guidelines issued by the Ethical Committee of Shanxi University (No. SXULL2024010). After a single-dose administration of AN–Cy7@BSA or AN–Cy7@HSA (48 μmol/L, 175 μL) *via* tail vein, the real-time imaging was carried out under a Bruker *In Vivo* FX Pro Imaging System. As shown in Figs. 2A and B, thanks to its high fluorescence brightness, AN–Cy7@HSA was found to exhibit obvious tumor accumulation on day 4, essentially reaching up to a maximum on day 5 with the tumor-to-normal tissue ratio (T/N ratio) calculated to be ~3.3 in the time point. In comparison, although AN–Cy7@BSA also showed certain tumor accumulation, its maximum mean fluorescence intensity at tumor site and maximum T/N ratio (~2.1 on day 4) were obviously lower than those of AN–Cy7@HSA (Fig. S17 in Supporting information). The strong fluorescence signal of AN–Cy7@HSA persisted at tumor site until day 8, which then gradually disappeared until day 16, meaning that the nanocomplex has a super-strong tumor accumulation and retention ability. Based on the observation, the time interval of day 4 to day 8 (five days) post intravenous injection (i.v.) of AN–Cy7@HSA was proposed as the time window for carrying out PDT. In addition, the *in vivo* imaging assays also revealed that AN–Cy7@HSA was metabolized mainly *via* liver, which was essentially completed on day 4. In view of the better tumor-targeting capability of AN–Cy7@HSA, the nanocomplex was selected for subsequent *in vivo* PDT studies.

The *in vivo* PDT assays of AN–Cy7@HSA were performed in the HepG2 tumor-bearing mouse models. These mice were divided into four groups, *i.e.*, PBS group (G1), PBS/light group (G2), AN–Cy7@HSA group (G3), and AN–Cy7@HSA/light group (G4), with three mice in each group. For AN–Cy7@HSA/light group, a single dose of AN–Cy7@HSA (48 μmol/L, 175 μL) was administrated *via* tail vein on day 0, and the tumors were irradiated by 750 nm laser (50 mW/cm^2, 60 min) on day 4 (Fig. 2C). After a single PDT treatment, the tumors in AN–Cy7@HSA/light group showed obvious shrinkage and scabbing over time (Fig. 2D), which were almost completely ablated on day 10, whereas tumors in control groups grew rapidly. After sacrifice of these mice, all tumors were excised. As seen in Fig. 2E, tumors in AN–Cy7@HSA/light group were almost undetectable, whereas tumors in other groups were obviously larger than their initial volumes. The high PDT efficacy was also confirmed by hematoxylin and eosin (HE) staining assays, where obvious tissue necrosis was observed in AN–Cy7@HSA/light group, whereas no extensive cell damage was found in control groups (Fig. 2F). After PDT treatment, the weights of the mice in AN–Cy7@HSA/light group almost unchanged, and no HE stain abnormality was observed in other major organs (Fig. S18 in Supporting information), indicative of the good biosafety of AN–Cy7@HSA nanocomplex. For more details, please refer to Fig. S19 in Supporting information. Further, we tested the photothermal effect of AN–Cy7@HSA by an infrared thermal imaging camera, and found that during a 30 min photoirradiation treatment, the temperature

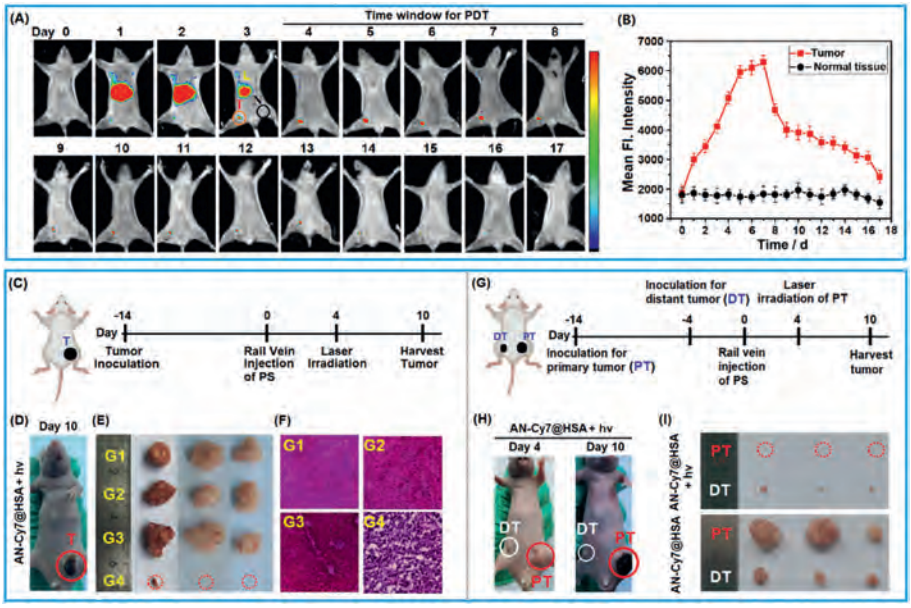


Fig. 2. (A) Time-dependent *in vivo* fluorescence imaging of HepG2 tumor-bearing BALB/c mice after i.v. of AN–Cy7@HSA nanocomplexes (48 μmol/L, 175 μL), and (B) the mean fluorescence intensity changes in tumor (red circle) and normal tissue (black circle) regions. Excitation filter: 760 nm; emission filter: 790 nm. Letters T, N, and L refer to tumor, normal tissue, and liver, respectively. Data are presented as mean ± SD ($n = 3$). (C) Schematic illustration of the schedule for tumor inoculation and AN–Cy7@HSA-mediated PDT of tumors. (D) Representative mouse image on day 10 showing the tumor morphology after PDT. (E) *Ex vivo* images of the tumors harvested from different groups on day 10 post i.v. of AN–Cy7@HSA. G1-G4 refer to PBS group, PBS/light group, AN–Cy7@HSA group, and AN–Cy7@HSA/light group, respectively. (F) HE staining of tumor tissues from different groups on day 6 post i.v. (G) Schematic illustration of the schedule for AN–Cy7@HSA-mediated *in vivo* PDT of primary tumor (PT) and antitumor immune response on distant tumor (DT). (H) Representative mouse images on day 4 and day 10 respectively showing the morphologies of primary tumor and distant tumor before and after PDT. (I) *Ex vivo* images of primary and distant tumors harvested from AN–Cy7@HSA/light and AN–Cy7@HSA groups on day 10, respectively, post i.v. of AN–Cy7@HSA on day 0 and PDT on day 4.

in tumor region was almost unchanged (Fig. S20 in Supporting information), meaning that AN–Cy7@HSA has a negligible photothermal effect for tumor. Finally, we evaluated the PDT-triggered immunotherapeutic effect of AN–Cy7@HSA [64–66]. The bilateral HepG2 tumor models were established by the subcutaneous inoculation of HepG2 cells on day −10 and day −4, respectively, before a single dose administration of AN–Cy7@HSA *via* tail vein on day 0 (Fig. 2G). On day 4, primary tumors (PT) in AN–Cy7@HSA/light group were irradiated by 750 nm laser, and no any treatment was performed for AN–Cy7@HSA group. At day 10, these mice were sacrificed and all tumors were excised. As shown in Figs. 2H and I, for AN–Cy7@HSA/light group, primary tumors were found to be ablated completely, and simultaneously the growth of distant tumors were effectively suppressed; in stark contrast, both primary and distant tumors grew obviously for AN–Cy7@HSA group. Also, we evaluated the PDT-triggered immunotherapeutic effect of AN–Cy7@HSA toward lung metastatic tumor (Fig. S21 in Supporting information). It was found that the anatomic lungs in AN–Cy7@HSA group show obvious pathological features, including lung enlargement, metastatic nodules, and lung consolidation; by comparison, the lungs in AN–Cy7@HSA/light group were all normal. Overall, after a single PDT treatment, AN–Cy7@HSA could not only ablate primary tumor but also trigger an antitumor immune response to suppress the growth of distant tumor.

In summary, a *meso*–anthranyl Cy7 PS is presented based on the SOCT-ISC mechanism, which exhibits a strong ability in generating $^1O_2$ under 750 nm photoirradiation while retaining strong emission at *ca.* 805 nm. The PS could form a 2:1 nanocomplex with HSA, and thus displays a strong accumulation ability at tumor site. *In vivo* PDT assays in mouse models reveal that, the nanocomplex almost completely ablates primary tumors, while triggering an antitumor immune response to suppress the growth of distant tumors.

Declaration of competing interest

The authors declare that they have no known competing financial interests or personal relationships that could have appeared to influence the work reported in this paper.

CRediT authorship contribution statement

Mengxing Liu: Writing – original draft, Validation, Software, Methodology, Investigation, Data curation. **Jing Liu:** Writing – original draft, Supervision, Project administration, Methodology, Investigation, Funding acquisition, Data curation, Conceptualization. **Hongxing Zhang:** Validation, Supervision, Project administration, Methodology, Investigation, Data curation, Conceptualization. **Lijuan Wang:** Validation, Investigation. **Jianan Tao:** Validation, Investigation. **Wei Guo:** Writing – review & editing, Supervision, Project administration, Methodology, Investigation, Funding acquisition, Conceptualization.

Acknowledgments

This work was supported by National Natural Science Foundation of China (Nos. 22277070, 22274091, 22007061), Fundamental Research Program of Shanxi Province (Nos. 20210302123445, 202403021211019), Science and Technology Innovation Talent Team Foundation of Shanxi Province (No. 202304051001002), Key Laboratory of Photochemical Functional Molecules in Shanxi Province, and Central and Local Scientific and Technological Foundation (No. Z135050009017).

Supplementary materials

Supplementary material associated with this article can be found, in the online version, at doi:10.1016/j.cclet.2025.111141.

References

[1] M. Ethirajan, Y. Chen, P. Joshi, R.K. Pa, Chem. Soc. Rev. 40 (2011) 340–362.
[2] X. Zhao, J. Liu, J. Fan, H. Chao, X. Peng, Chem. Soc. Rev. 50 (2021) 4185–4219.
[3] X. Li, N. Kwon, T. Guo, Z. Liu, J. Yoon, Angew. Chem. Int. Ed. 57 (2018) 11522–11531.
[4] T.C. Pham, V. Nguyen, Y. Choi, S. Lee, J. Yoon, Chem. Rev. 121 (2021) 13454–13619.
[5] M. Li, Y. Xu, X. Peng, J.S. Kim, Acc. Chem. Res. 55 (2022) 3253–3264.
[6] Z. Wang, A. Wu, W. Cheng, et al., Nat. Commun. 14 (2023) 7251.
[7] D. Huang, J. Yin, Y. Zou, et al., Smart Mol. 2 (2024) e20240005.
[8] J.H. Correia, J.A. Rodrigues, S. Pimenta, T. Dong, Z. Yang, Pharmaceutics 13 (2021) 1332.
[9] X. Xiao, K. Ye, M. Imran, J. Zhao, Appl. Sci. 12 (2022) 9933.
[10] V. Nguyen, Y. Yan, J. Zhao, J. Yoon, Acc. Chem. Res. 18 (2021) 207–220.
[11] M.A. Filatov, Org. Biomol. Chem. 18 (2020) 10–27.
[12] P. Chinna Ayya Swamy, G. Sivaraman, R.N. Priyanka, et al., Coord. Chem. Rev. 411 (2020) 213233.
[13] A.P. Castano, T.N. Demidova, M.R. Hamblin, Photodiagn. Photodyn. Ther. 1 (2004) 279–293.
[14] S.M. Usama, S. Thavornpradit, K. Burgess, ACS Appl. Bio. Mater. 1 (2018) 1195–1205.
[15] J.L. Bricks, A.D. Kachkovskii, Y.L. Slominskii, A.O. Gerasov, S.V. Popov, Dye. Pigm. 121 (2015) 238–255.
[16] Z. Chang, F. Liu, L. Wang, et al., Chin. Chem. Lett. 30 (2019) 1856–1882.
[17] W. Sun, S. Guo, C. Hu, J. Fan, X. Peng, Chem. Rev. 116 (2016) 7768–7817.
[18] Y. Liao, Y. Liang, Y. Huang, et al., Chin. Chem. Lett. 35 (2024) 109092.
[19] X. Zhang, Y. Qin, H. Zhang, et al., Chin. Chem. Lett. 36 (2025) 110715.
[20] X. Luo, J. Li, J. Zhao, et al., Chin. Chem. Lett. 30 (2019) 839–846.
[21] L. Zhou, Z. Wang, L. Wang, X. Zhang, Y. Xiao, J. Am. Chem. Soc. 145 (2023) 28296–28306.
[22] G. Jo, E.J. Kim, H. Hyun, Int. J. Mol. Sci. 24 (2023) 862.
[23] S.M. Usama, G.K. Park, S. Nomura, et al., Bioconjug. Chem. 31 (2020) 248–259.
[24] S.M. Usama, C.M. Lin, K. Burgess, Bioconjug. Chem. 29 (2018) 3886–3895.
[25] S. Luo, X. Luo, X. Wang, et al., Small 18 (2022) 2201298.
[26] Y. Xu, W. Zhou, L. Xiao, et al., ACS Omega 7 (2022) 33821–33829.
[27] L. Xu, S.B. Xu, C. Wang, et al., ACS Appl. Mater. Interfaces 11 (2019) 38385–38394.
[28] Z. Liu, X. Chen, Chem. Soc. Rev. 45 (2016) 1432–1456.
[29] E.N. Hoogenboezem, C.L. Duvall, Drug Deliv. Rev. 130 (2018) 73–89.
[30] R. Solanki, H. Rostamabadi, S. Patel, S.M. Jafari, Int. J. Biol. Macromol. 193 (2021) 528–540.
[31] R. Tovtik, E. Muchová, L. Stacková, P. Slavícek, P. Klán, J. Org. Chem. 88 (2023) 6716–6728.
[32] J. Atchison, S. Kamila, H. Nesbitt, et al., Chem. Commun. 53 (2017) 2009–2012.
[33] I. Noh, D. Lee, H. Kim, et al., Adv. Sci. 5 (2018) 1700481.
[34] J. Cao, J. Chi, J. Xia, et al., ACS Appl. Mater. Interfaces 11 (2019) 25720–25729.
[35] S. Siriwibool, N. Kaekratoke, K. Chansaenpak, et al., Sci. Rep. 10 (2020) 1283.
[36] X. Zhao, S. Long, M. Li, et al., J. Am. Chem. Soc. 142 (2020) 1510–1517.
[37] Y. Liu, J. Zhang, X. Zhou, et al., Angew. Chem. Int. Ed. 63 (2024) e202408064.
[38] O. Semenova, D. Kobzev, F. Yazbak, et al., Dyes Pigm. 195 (2021) 109745.
[39] W. Liu, S. He, X. Ma, et al., Angew. Chem. Int. Ed. 63 (2024) e202411802.
[40] L. Jiao, F. Song, J. Cui, X. Peng, Chem. Commun. 54 (2018) 9198–9201.
[41] S. Luo, X. Tan, S. Fang, et al., Adv. Funct. Mater. 26 (2016) 2826–2835.
[42] X. Zhao, H. Zhao, S. Wang, et al., J. Am. Chem. Soc. 143 (2021) 20828–20836.
[43] Y. Xu, J. Yu, J. Hu, et al., Adv. Healthc. Mater. 12 (2023) 2203080.
[44] T. Liu, Y. Chen, H. Wang, et al., Adv. Healthc. Mater. 12 (2023) 2202817.
[45] E.M.S. Stennett, M.A. Ciuba, M. Levitus, Chem. Soc. Rev. 43 (2014) 1057–1075.
[46] M.A. El-Sayed, J. Chem. Phys. 50 (1974) 4502–4507.
[47] M.A. Filatov, S. Karuthedath, P.M. Polestshuk, et al., J. Am. Chem. Soc. 139 (2017) 6282–6285.
[48] Z. Wang, J. Zhao, Org. Lett. 19 (2017) 4492–4495.
[49] K. Chen, W. Yang, Z. Wang, et al., J. Phys. Chem. A 121 (2017) 7550–7564.
[50] Z.E.X. Dance, S.M. Mickley, T.M. Wilson, et al., J. Phys. Chem. 112 (2008) 4194–4201.
[51] J.T. Buck, A.M. Boudreau, A. DeCarmine, et al., Chem. 5 (2019) 138–155.
[52] M. Lv, Y. Yu, M.E. Sandoval-Salinas, et al., Angew. Chem. Int. Ed. 59 (2020) 22179–22184.
[53] Y. Hou, Q. Liu, J. Zhao, Chem. Commun. 56 (2020) 1721–1724.
[54] Z. Wang, M. Ivanov, Y. Gao, et al., Chem. Eur. J. 26 (2020) 1091–1102.
[55] J. Miao, Y. Huo, G. Yao, et al., Angew. Chem. Int. Ed. 61 (2022) e202201815.
[56] J. Miao, G. Yao, Y. Huo, et al., ACS Appl. Mater. Interfaces 16 (2024) 40428–40443.
[57] D. Xi, N. Xu, X. Xia, et al., Adv. Mater. 34 (2021) 2106797.
[58] X. Zhao, Q. Yao, S. Long, et al., J. Am. Chem. Soc. 143 (2021) 12345–12354.
[59] X. Zhao, S. He, W. Chi, et al., Adv. Sci. 9 (2022) 2202885.
[60] M. Liu, J. Liu, H. Zhang, et al., Chin. Chem. Lett. 36 (2025) 109994.
[61] R. Li, B. Ma, M. Li, et al., Chem. Sci. 15 (2024) 11408–11417.
[62] X. Lv, T. Han, X. Yuan, H. Shi, W. Guo, Analyst 146 (2021) 64–68.
[63] N. Lange, W. Szlasa, J. Saczko, A. Chwiłkowska, Pharmaceutics 13 (2021) 818.
[64] H. Ma, Y. Lu, Z. Huang, et al., J. Am. Chem. Soc. 144 (2022) 3477–3486.
[65] Z. Yi, X. Qin, L. Zhang, et al., J. Am. Chem. Soc. 146 (2024) 9413–9421.
[66] W. Zhen, D.W. Kang, Y. Fan, et al., J. Am. Chem. Soc. 146 (2024) 16609–16618.